

Title: Asymmetry of resonance Raman profiles in semiconducting single-walled carbon nanotubes at the first excitonic transition

Author(s): Gordeev, G., Flavel, B., Krupke, R., Kusch, P., & Reich, S.

Document type: Postprint

Terms of Use: Copyright applies. A non-exclusive, non-transferable and limited right to use is granted. This document is intended solely for personal, non-commercial use.

Citation: Gordeev, G., Flavel, B., Krupke, R., Kusch, P., & Reich, S. (2019). Asymmetry of resonance Raman profiles in semiconducting single-walled carbon nanotubes at the first excitonic transition. *Physical Review B*, 99(4). <https://doi.org/10.1103/physrevb.99.045404>

Asymmetry of resonance Raman profiles in semiconducting single-walled carbon nanotubes at the first excitonic transition

Georgy Gordeev,^{1, a)} Benjamin Flavel,^{2,3} Ralph Krupke,^{2,3} Patryk Kusch,¹ and Stephanie Reich¹

¹⁾*Department of Physics, Freie Universität Berlin, Arnimallee 14, 14195 Berlin, Germany.*

²⁾*Institute of Nanotechnology, Karlsruhe Institute of Technology, Karlsruhe, Germany.*

³⁾*Institute of Materials Science, Technische Universität Darmstadt, Darmstadt, Germany.*

(Dated: 19 December 2018)

Carbon nanotubes are one-dimensional nanoscale systems with strongly pronounced chirality dependent optical properties with multiple excitonic transitions. We investigated the high-energy G mode of semiconducting single walled nanotubes of different chiralities at first excitonic transition by applying resonant Raman spectroscopy. The G mode intensity dependence on excitation energy yielded asymmetric resonance Raman profiles similar to ones we reported for the second excitonic transition. We found the scattering efficiency to be strongest at the incoming Raman resonance. Still, the degree of asymmetry is different for the first and second transitions and the first transition profiles provide a narrower line shape due to longer exciton lifetimes. The overall scattering efficiency is up to a factor of 25 times more intense at first excitonic transition, compared to the second transition. The fifth-order perturbation theory, with implemented phonon scattering pathways between excitonic states, excellently reproduced experimental data.

PACS numbers: Valid PACS appear here

Keywords: carbon nanotubes, resonant Raman, first excitonic transition, exciton-phonon coupling

I. INTRODUCTION

Single walled carbon nanotubes are unique 1D crystals with outstanding vibrational and mechanical properties^{1,2}. The excitons with high binding energies (up to 1eV in vacuum) rule the optical properties of the nanotubes^{3,4}. The low-dimensional electron-hole interaction in carbon nanotubes gives a rise to the dark and bright excitonic states^{5,6}, providing a strong coupling with the lattice vibrations (phonons)⁷. Spectroscopic features originating from the coupling of the momentum-forbidden dark excitons and the K point phonons were reported in a variety of optical studies. Characteristic phonon related peaks occur in the carbon nanotube absorbance, photoluminescence and photoconductivity spectra⁸⁻¹⁰.

In Raman scattering the remarkably strong exciton-phonon coupling induces higher order scattering processes¹¹. The standard third-order Raman process with the emission of a Γ -point phonon couples only to the bright excitonic state. The fourth-order process does not contribute to one-phonon Raman scattering. The fifth-order process, however, opens phonon-mediated scattering channels between the different excitonic states¹¹. A unique type of asymmetry in the resonance Raman profile of the G mode is due to these scattering channels^{11,12}. The degree of asymmetry depends on the coupling efficiency between the bright and dark excitonic states. This asymmetry was previously ascribed to the alternative

theories based on molecular-like non-Condon effects¹² and interferences between electronic bands¹³. However, these theories do not accurately treat excitonic nature of optical excitations in the nanotube.

Previous experiments by others as well as our own studies focused on the asymmetry in the resonance profile at the second excitonic transition (E_{22}) of semiconducting nanotubes^{12,14}. However, the second excitonic state is located inside of the uncorrelated electron hole (e-h) continuum of the first excitonic transition which can contribute to the scattering efficiency. Such interactions were reported for three-dimensional crystals, with excitonic properties¹⁵. The lowest energy excitonic transition (E_{11}) provides the cleanest excitonic level where the interference with uncorrelated e-h pairs (higher excitonic states) is impossible due to the large binding energy of the excitonic state^{3,4}. The resonant Raman study of the first transition is essential to clarify the origin of the asymmetry.

The comparison between the asymmetry in resonance Raman profiles between the E_{22} and the E_{11} transitions will clarify two main controversies found in the literature surrounding this subject. First, to understand if the lack of the asymmetry reported for the E_{33} transition is related to the high transition number or the large diameter of the investigated nanotube¹⁶. Second, the validity of the alternative theory attributing the asymmetry to the displacement of the nuclear coordinate can be tested based on its predictions for the transition number dependence¹².

Complementary to the asymmetry effect in resonance Raman profiles, the width and absolute scattering efficiency are due to the coherent excitonic lifetime and

^{a)}Electronic mail: gordeev@zedat.fu-berlin.de

exciton-phonon coupling strength respectively. The resonant Raman study of radial breathing modes (RBMs) at the first and second excitonic transitions reported strong enhancement of the Raman intensity up to $3 \cdot 10^2$ times accompanied by the reduced width of the resonance Raman profile of the E_{11} transition compared to the E_{22} transition¹⁷. The potential enhancement of the G mode intensity at the first transition will be of interest for possible biomedical applications. The higher intensity simplifies detection process and the first transition of small diameter tubes covers the transparency region of tissue¹⁸. In this wavelength range (700 - 1350 nm), the localization and vibrational properties of CNTs, serving as markers or transporters^{19,20}, can be probed without disturbing or damaging the living cells.

Despite the fundamental interest in Raman scattering of semiconducting CNTs at E_{11} , only a few experimental works reporting RBM intensities have been published^{17,21}. In contrast to the RBM, the frequency of the G band depends only weakly on nanotube chirality. The G mode of different species cannot be separated in samples containing tubes of different chirality. The techniques providing to obtain samples of high chiral purity were only recently developed^{22,23}. Moreover, measuring the E_{22} and E_{11} G mode resonances profiles of the single nanotube chirality requires a very broad excitation source and multiple detection instruments.

Here, we report a complete study of the high-energy modes at the E_{11} transition by applying resonant Raman spectroscopy. We investigated the transition dependence of resonance Raman profiles. At the first transition all studied chiralities demonstrated a narrower width of Raman profiles compared to the second transition and showed a dominant incoming resonance. The degree of asymmetry varied between profiles at first and second transitions. A fifth-order perturbation theory model involving the scattering to dark excitonic states describes the Raman profiles quite well. We observed an increase of the G mode Raman intensity with a maximum factor of 25. The increase of the intensity and the change in asymmetry we attribute to the strengthening of the dark and bright exciton-phonon interactions at the first excitonic state.

II. EXPERIMENTAL

The single chirality samples (6,4), and (8,3) were enriched by a gel permeation chromatography method²³. The ambient conditions and surfactant concentration were optimized to preferably absorb a particular chirality to the gel. The obtained nanotubes were covered with sodium dodecyl sulfate (SDS) and suspended in aqueous solution²⁴. The purity of the samples was confirmed by absorption, photoluminescence-excitation, and resonant Raman spectroscopy^{14,23}. The chiral purity of the samples reached up to 95 %.

For resonant Raman scattering studies we used a sin-

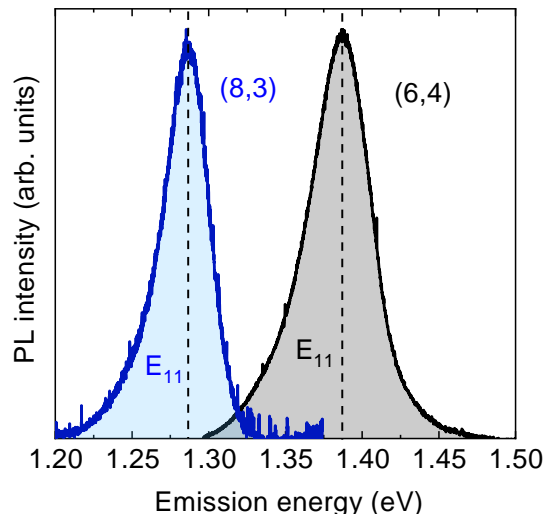


FIG. 1. The E_{11} photoluminescence spectra of the (8,3) and (6,4) samples excited at 1.96 and 2.11 eV respectively.

TABLE I. Nanotube chirality and $v = |n - m| \bmod 3$ type, nanotube diameter d , chiral angle θ and resonant energies of bright (E_B^1) and dark excitons (E_D^1) established from the PL and Vora *et al.*¹⁰

(n,m)	v index	d (Å)	θ (deg)	E_B^1 , (eV)	E_D^1 , (eV)
(6,4)	-1	6.83	23.4	1.39	1.424
(8,3)	-1	7.72	15.3	1.29	1.323

gle frequency Ti:Sapphire laser (700-1000nm). A Horiba T64000 in macro configuration set up was used, with a lens (N.A. = 0.8) focusing (collecting) the incident (scattered) light onto the suspended nanotubes. The scattered light of wavelengths below 1050 nm was analyzed by a triple grating spectrometer (Horiba T64000) equipped with a silicon CCD and 600 grooves per mm grating with the spectral resolution $< 4 \text{ cm}^{-1}$ at 1.45 eV. We analyzed the scattered light with wavelengths above 1050 nm by guiding it through the fiber in an iHR Horiba spectrometer, equipped with a 150 grooves per mm grating and detected by an InGaAs array. The intensity of the Raman mode was calibrated on the benzonitrile molecule recorded with the same experimental geometry. Benzonitrile has a constant Raman cross section in the visible and infra-red regions^{12,25}.

For the modelling of the Raman resonance profiles the position of the bright exciton needs to be established. The E_{11} photoluminescence (PL) peak was recorded for each chirality in the above-described set up and calibrated with a neon spectrum. The tubes are excited at E_{22} using a dye laser (R6G, DCM) (560-680nm). Figure 1 shows the PL spectra of (6,4), and (8,3) tubes. The maximum of the PL corresponds to the energy of the allowed bright excitonic transition E_B^1 . By fitting the PL profiles, the E_B^1 were determined and are listed in

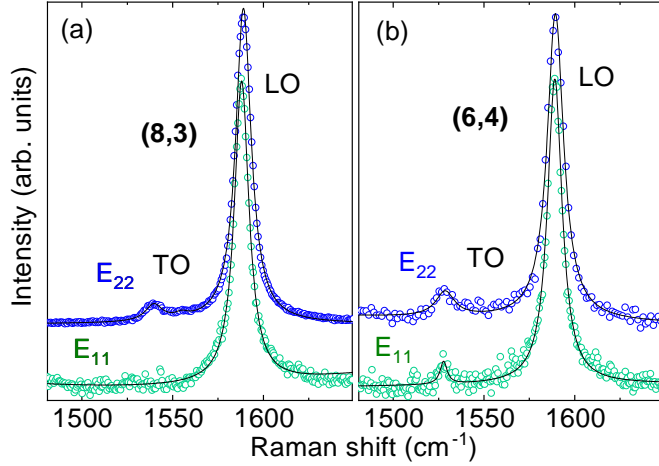


FIG. 2. The G modes of the (6,4) and (8,3) SWCNTs at the first (bottom spectra) and the second excitonic transition (top spectra). Solid lines represent fits with Lorentzian line shapes.

TABLE II. Chirality (n,m) and transition E_{ii} dependent intensity ratios between TO and LO phonons, full width at half maxima (FWHM) of the TO and LO phonons

(n,m)	E_{ii}	I_{TO}/I_{LO}	LO FWHM, cm^{-1}	TO FWHM, cm^{-1}
(6,4)	E_{22}	0.06	11	8
(6,4)	E_{11}	0.03	10	4
(8,3)	E_{22}	0.06	10	11
(8,3)	E_{11}	0	10	

Table I. The measured transition energies are in a good agreement with previously reported values^{21,26}. In order to determine the energy of the dark excitonic states at E_D^{11} we use the energy separation between the bright and dark excitonic states 33 and 34 meV for the (6,4) and the (8,3) nanotubes, respectively. These values are reported in experimental photoluminescence-excitation studies¹⁰.

III. RESULTS AND DISCUSSION

Before discussing the resonant effects, we outline the differences in the G mode structure between the second and the first transitions. Figure 2 shows normalized Raman spectrum of the G mode excited at the first (bottom spectra) and the second (top spectra) excitonic transitions for two different nanotube chiralities (6,4), and (8,3). The component (G^+) at 1589 cm^{-1} is the longitudinal optical vibration (LO), the weak component (G^-) at 1521 cm^{-1} in the (6,4) and 1540 cm^{-1} in the (8,3) nanotube is the transverse vibration (TO). The corresponding frequencies and LO/TO intensity ratios match well with the reported theoretical and experimental values for the second excitonic transition^{25,27,28}. The I_{TO}/I_{LO} are listed in Table II.

At E_{11} we observe different I_{TO}/I_{LO} ratios compared

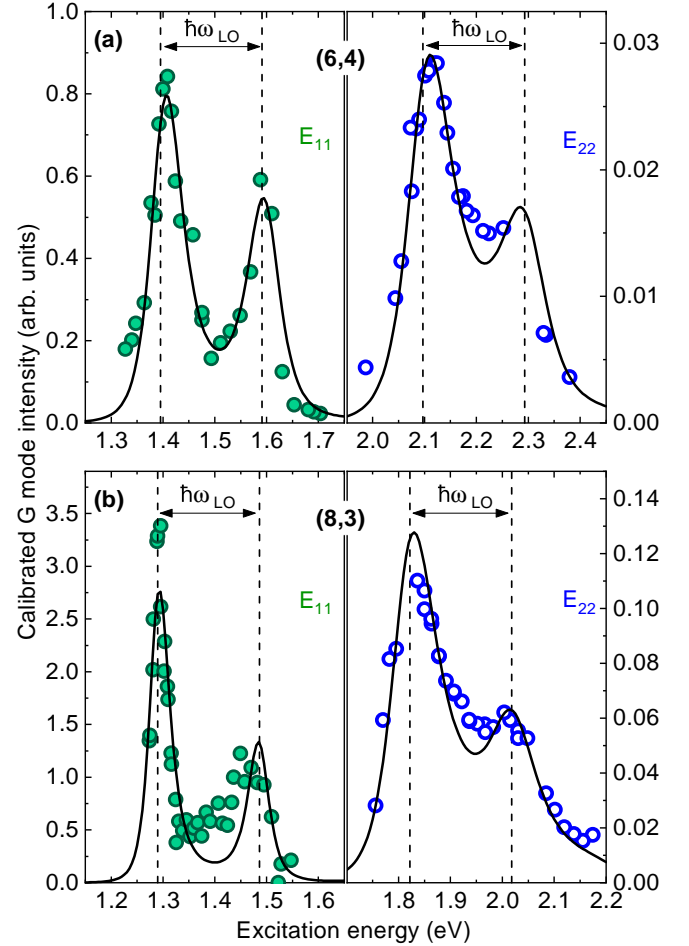


FIG. 3. (a), (b) resonance Raman profiles of the LO mode of the (6,4), and (8,3) nanotubes respectively. The filled (open) symbols indicate the intensity (integrated peak area) of the G mode excited in first (second) excitonic transition. E_{22} data are extracted from Gordeev *et al.*¹⁴. The calibration of Raman intensity is described in the experimental section. The solid lines represent theoretical resonance Raman profiles by Eq. (1).

to E_{22} , such that the ratio decreases in the (6,4) and (8,3) nanotubes [$v = -1$ type]. The TO intensity of the (8,3) is even below the instrumental noise level. An increase of the I_{TO}/I_{LO} with chiral angle at first excitonic transition is similar to the trend reported for the E_{22} transition^{25,27}.

To gain further insight into the Raman scattering mechanisms, we investigate the intensity (integrated peak area) dependence of the LO mode on excitation energy. For each nanotube we evaluated the intensity of the Raman mode as a function of excitation wavelengths. We compare the resonance Raman profiles at the first E_{11} and second E_{22} excitonic transitions in Figure 3 a and b. The filled symbols represent modes intensity excited via E_{11} and the open symbols via the E_{22} , reported by Gordeev *et al.*¹⁴. The Raman profile comprises of two resonances; an incoming resonance at E_{ii}^B , and an outgo-

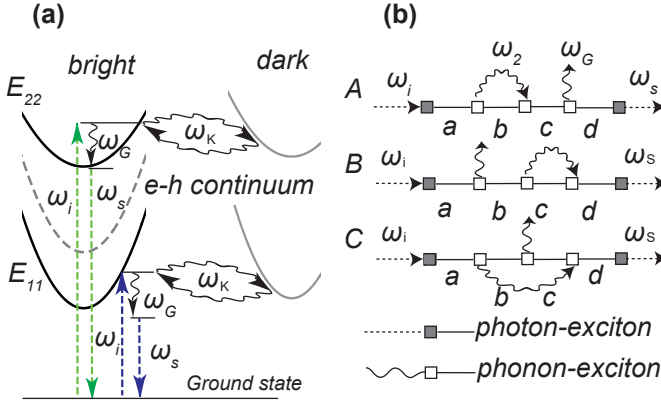


FIG. 4. (a) The scheme demonstrating one of possible scattering pathway (A), the bright (dark) E_{11} and E_{22} states are located at the Γ (K) point of Brillouin Zone. (b) Feynman diagrams summing up fifth-order scattering possibilities, as ω_2 phonon serves ω_K (ω_G) when scattering occurs between bright-dark (bright-bright) excitonic states.

ing resonance at $E_{ii}^B + \hbar\omega_{LO}$ (marked by the dashed lines), where E_{ii}^B and $\hbar\omega_{LO}$ are the energies of the bright exciton and phonon, respectively. Both incoming and outgoing resonances have narrower line shapes at the E_{11} than at the E_{22} transition.

The different intensities of the incoming and outgoing resonances (asymmetry) observed at the E_{22} resonances distinguishes nanotubes from most other crystalline materials²⁹. The asymmetry is also observed in resonance with the E_{11} transition, again with dominating incoming resonance. The degree of asymmetry varies with transition number and chirality. We observe the resonance Raman profile of the (6,4) species to be more symmetric at E_{11} than at E_{22} (Fig. 3a and b), whereas

the (8,3) profile becomes more asymmetric at E_{11} compared to E_{22} (Fig. 3b).

The relative intensity of the LO mode at E_{11} is up to 25 times higher at the incoming resonance varying with tube chirality, see Table III. To understand the shape of the resonance Raman profiles and the changes in scattering efficiencies between different exciton transitions, we analyze the experimental results in the framework of fifth-order Raman scattering including phonon interactions between bright and dark excitonic states mediated by phonons¹¹. This model excellently reproduced Stokes and anti-Stokes Raman profiles of semiconducting nanotubes at E_{22} and Stokes resonance profiles as well as in metallic nanotubes at the E_{11} transition^{11,14}.

The higher order Raman processes are considered, as the standard third-order Raman process including photon absorption and emission and one phonon emission is insufficient to reproduce the excitation energy dependence of the G modes intensities. The high exciton-phonon coupling enables additional scattering channels connecting bright and dark excitonic states^{12,14}. Such processes contain two additional steps describing the emission and absorption of K (G)-point phonons. The K (G) phonon couples the bright to dark (bright) excitonic state. The scheme corresponding to one of the scattering pathways (A) is shown in Figure 4a. Each bright excitonic state at the Γ point of the Brillouin zone is scattered to its dark counterpart at the K point by a finite momentum phonon. In this scattering pathway, first the bright exciton is scattered by the K phonon to the dark state and back first and after that, the G phonon is emitted. The order of single scattering events can vary, resulting in two additional scattering pathways (B, C). These pathways are presented in form of Feynman diagrams in Figure 4b. Phonon interferences alter the Raman cross section resulting in $I_G \sim |W_G|^2$,¹¹ with

$$\begin{aligned}
 W_G(E_L) = & \frac{|(M_{BGS}^{XL})_{ii}|^2 (M_G^{XP})_{ii}}{(E_{BGS}^{ii} - E_L)(E_{BGS}^{ii} + \hbar\omega_G - E_L)} \left(1 + \frac{|(M_G^{XP})_{ii}|^2}{(E_{BGS}^{ii} + 2\hbar\omega_G - E_L)(E_{BGS}^{ii} + \hbar\omega_G - E_L)} \right. \\
 & + \frac{|(M_G^{XP})_{ii}|^2}{(E_{BGS}^{ii} - E_L)(E_{BGS}^{ii} + \hbar\omega_G - E_L)} + \frac{|(M_K^{XP})_{ii}|^2}{(E_{DKS}^{ii} + \hbar\omega_G + \hbar\omega_K - E_L)(E_{BGS}^{ii} + \hbar\omega_G - E_L)} \\
 & \left. + \frac{|(M_K^{XP})_{ii}|^2}{(E_{DKS}^{ii} + \hbar\omega_G + \hbar\omega_K - E_L)(E_{BGS}^{ii} + \hbar\omega_K - E_L)} + \frac{|(M_K^{XP})_{ii}|^2}{(E_{BGS}^{ii} - E_L)(E_{DKS}^{ii} + \hbar\omega_K - E_L)} \right)
 \end{aligned} \quad (1)$$

M^{XL} is the exciton-photon and M^{XP} the exciton-phonon matrix element, specific for each ii transition. The energy of the bright exciton is expressed as $E_{BGS}^{ii} = E_B^{ii} + i\Gamma_B/2$ and the energy of the dark exciton as $E_{DKS}^{ii} = E_D^{ii} + i\Gamma_D/2$ at corresponding excitonic transition E_{ii} . Γ_B (Γ_D) is the damping parameter propor-

tional to the inverse lifetime of the bright (dark) exciton. $\hbar\omega_G = 0.196$ eV (Fig. 2), ($\hbar\omega_K = 0.17$ eV)¹⁰ is the phonon energy of the LO phonon at the Γ (K) point of the Brillouin zone.

The energies of the bright and dark excitons established in the experimental section were used for the fit-

TABLE III. Intensity ratio of the LO phonon between transitions. The ratios between dark exciton-phonon and bright exciton-phonon matrix elements for the first and second excitonic transitions¹⁴, damping parameters for the bright and dark excitons and bright exciton-photon/ bright exciton-phonon matrix elements obtained by fitting the experimental resonance profiles by Eq. (1) for E_{11} and extracted from Gordeev *et al.*¹⁴ for E_{22}

(n,m)	$\frac{I_{11}}{I_{22}}$	$(\frac{M_K^{XP}}{M_G^{XP}})_{11}$	$(\frac{M_K^{XP}}{M_G^{XP}})_{22}$	$(\Gamma_B/2)_{11}$, meV	$(\Gamma_B/2)_{22}$, meV	$(M_{BTS}^{XL})_{11}$, meV	$(M_G^{XP})_{11}$, meV	$(\Gamma_D/2)_{11}$, meV
(6,4)	24	1.8	2.1	54	90	56	715	680
(8,3)	15	3	1	35	84	13	700	3244

ting of the experimental data by using the matrix elements and exciton damping energies as free parameters. The resonance Raman profiles (depicted by solid lines in Figures 3a and 3b) are in good agreement with the experimental data (symbols). The relative coupling strength between bright and dark excitons is defined by the ratio of the exciton phonon matrix elements $(M_K^{XP}/M_G^{XP})_{ii}$. Together with Γ_B it determines the asymmetry of Raman profiles; the values are given in Table III. In the (6,4) nanotube the ratio does not significantly change. The increase of symmetry at the E_{11} transition is due to the reduction of the excitonic lifetime. In the (8,3) nanotube, Γ_B follows the same trend as in the (6,4) nanotube, but $(M_K^{XP}/M_G^{XP})_{11}$ exceeds $(M_K^{XP}/M_G^{XP})_{22}$ by a factor of three, causing a higher asymmetry of the (8,3) E_{11} resonance profile, see Fig. 3.

The relative ratio between the bright exciton-phonon and the dark exciton-phonon matrix elements affects the asymmetry of resonance Raman profile, whereas the change of the bright exciton matrix element M_G^{XP} enhances or decreases the absolute Raman intensity. This effect is directly observed in Figure 2b, where the TO/LO intensity ratio dramatically decreases in the (8,3) nanotubes at the E_{11} transition indicating a decrease of $(M_{TO}^{XP})/(M_{LO}^{XP})$ at E_{11} compared to the E_{22} transition.

The quantitative behavior of M_{LO}^{XP} can be extracted from the measured profiles at E_{11} and E_{22} transition due to the uniform intensity calibration. M_{LO}^{XP} increases approximately by a factor of four from the second to the first transitions, inducing an increase in Raman intensity by up to factor of 25 at E_{11} , see Fig.3. This estimate is based on the exciton-photon matrix element M_{BTS}^{XL} tight binding calculations²⁷. When moving from the first to the second transition it increases by 15 %²⁷.

The resonance Raman profile at the E_{11} transition are narrower in frequency compared to the E_{22} transition. The change of the width in the resonance Raman profiles widths is related to the variation of the damping parameters (Γ_B), in Eq. (1). The damping parameters at the E_{22} transition are up to factor of two stronger than at E_{11} , see Table III. The damping parameter is inversely proportional to the exciton lifetime $\Gamma_B \sim 1/\tau$. The second exciton lies at higher energy and has higher number of radiative and non-radiative relaxation pathways when compared to the lowest E_{11} excitonic state³⁰. This explains the smaller exciton lifetime and broader Raman profile at E_{22} compared to the E_{11} transition.

The resonance Raman profiles exhibit asymmetry and are well fitted by fifth-order perturbation theory. This indicates that the scattering at both transitions (E_{11} and E_{22}) is ruled by the same phonon mediated interactions with dark states. The interference of the second transitions with uncorrelated e-h pairs is negligible, possibly due to the low oscillator strength of such uncoupled pairs. The lack of asymmetry reported for resonance Raman profile at the third transition is unlikely due to the high transition¹⁶, as we did not observe any qualitative differences in the profiles by varying the transition. Rather this effect is related to the high diameter of this species. The diameter dependence of the $(M_K^{XP}/M_G^{XP})_{ii}$ may be a key factor here.

The alternative theory for explaining the asymmetry of resonance Raman profiles is based on molecular system, where the atom displacement along the phonon oscillating direction induces non-Condon effects¹². This model fits well with the Stokes resonance profiles at second excitonic transition. It predicts an increase (decrease) of non-Condon parameter C moving from the second to the first transition in $v = +1$ ($v = -1$) type nanotubes. The non-Condon parameter is proportional to the asymmetry¹². However, we observe the varying trends in our experiment, where asymmetry decreases in one $v = -1$ (6,4) nanotube and increases in the other $v=-1$ (8,3) nanotube at the E_{22} transition, compared to the E_{11} transition.

IV. CONCLUSION

In conclusion, we studied the resonance Raman profiles in several nanotubes when exciting the G mode in resonance with the E_{11} transition. The resonance profiles of the LO phonon are similar to E_{22} we reported earlier. We observe asymmetric profiles with unequal incoming and outgoing resonances, where the incoming resonance dominates. We found the asymmetry of Raman profile to depend on the nanotubes chirality and transition number. The (6,4) profile is more symmetric and the (8,3) is more asymmetric at the E_{11} transition compared to the E_{22} transition. We attribute the asymmetry to the fifth-order scattering process and find excellent agreement between the experimental data and fit of the E_{11} and E_{22} Raman profiles. The change of asymmetry is due to a competing increase of the bright and dark exciton-phonon coupling elements. Overall, the Raman

scattering at the E_{11} transition is, by a factor of 25, more intense than for the E_{22} transition. The superior Raman intensity makes the excitation region of the first transition even more attractive for probing CNTs by means of Raman scattering in all application requiring strong Raman signals. We observe narrower resonance Raman profiles at first excitonic transition attributed to the long lifetime of the lowest-energy exciton.

ACKNOWLEDGMENTS

We gratefully acknowledge the German Research Foundation (DFG via SFB 658, subproject A6). We thank Sabrina Jürgensen for help with assembling resonance Raman spectrometer for the infra-red measurements.

- ¹S. Reich, C. Thomsen, and J. Maultzsch, *Carbon Nanotubes: Basic Concepts and Physical Properties* (WILEY-VCH, New York, 2004).
- ²A. Jorio, R. Saito, G. Dresselhaus, and M. S. Dresselhaus, *Raman Spectroscopy in Graphene Related Systems* (WILEY-VCH, Weinheim, 2011).
- ³F. Wang, G. Dukovic, L. E. Brus, and T. F. Heinz, *Science* **308**, 838 (2005).
- ⁴J. Maultzsch, R. Pomraenke, S. Reich, E. Chang, D. Prezzi, A. Ruini, E. Molinari, M. S. Strano, C. Thomsen, and C. Lienau, *PHYSICAL REVIEW B* **72**, 241402 (2005).
- ⁵V. Perebeinos, J. Tersoff, and P. Avouris, *Nano Lett* **5**, 2495 (2005).
- ⁶P. Avouris, M. Freitag, and V. Perebeinos, *Nature Photonics* **2**, 341 (2008).
- ⁷V. Perebeinos, J. Tersoff, and P. Avouris, *Physical Review Letters* **94**, 027402 (2005).
- ⁸O. N. Torrens, M. Zheng, and J. M. Kikkawa, *Phys Rev Lett* **101**, 157401 (2008).
- ⁹X. Qiu, M. Freitag, V. Perebeinos, and P. Avouris, *Nano Lett* **5**, 749 (2005).
- ¹⁰P. M. Vora, X. Tu, E. J. Mele, M. Zheng, and J. M. Kikkawa, *PHYSICAL REVIEW B* **81**, 155123 (2010).
- ¹¹E. H. Háróz, J. G. Duque, E. B. Barros, H. Telg, J. R. Simpson, A. R. Hight Walker, C. Y. Khripin, J. A. Fagan, X. Tu, M. Zheng, J. Kono, and S. K. Doorn, *PHYSICAL REVIEW B* **91**, 205446 (2015).
- ¹²J. G. Duque, H. Chen, A. K. Swan, A. P. Shreve, S. Kilina, S. Tretiak, X. Tu, M. Zheng, and S. K. Doorn, *ACS Nano* **5**, 5233 (2011).
- ¹³L. G. Moura, M. V. O. Moutinho, P. Venezuela, C. Fantini, A. Righi, M. S. Strano, and M. A. Pimenta, *PHYSICAL REVIEW B* **89**, 035402 (2014).
- ¹⁴G. Gordeev, A. Jorio, P. Kusch, B. G. M. Vieira, B. Flavel, R. Krupke, E. B. Barros, and S. Reich, *Physical Review B* **96**, 245415 (2017).
- ¹⁵A. Cantarero, C. Trallero-Giner, and M. Cardona, *Physical Review B* **39**, 8388 (1989).
- ¹⁶T. T. Tran, C. Elbadawi, D. Totonjian, C. J. Lobo, G. Grosso, H. Moon, D. R. Englund, M. J. Ford, I. Aharonovich, and M. Toth, *ACS Nano* (2016), 10.1021/acsnano.6b03602.
- ¹⁷B. C. Satishkumar, S. V. Goupalov, E. H. Haroz, and S. K. Doorn, *PHYSICAL REVIEW B* **74**, 155409 (2006).
- ¹⁸A. M. Smith, M. C. Mancini, and S. Nie, *Nature Nanotechnology* **4**, 710 (2009), arXiv:NIHMS150003.
- ¹⁹S. Beg, M. Rizwan, A. M. Sheikh, M. S. Hasnain, K. Anwer, and K. Kohli, *Journal of Pharmacy and Pharmacology* **63**, 141 (2011).
- ²⁰E. Heister, V. Neves, C. Tilmaciú, K. Lipert, V. S. Beltrán, H. M. Coley, S. R. P. Silva, and J. McFadden, *Carbon* **47**, 2152 (2009).
- ²¹H. Telg, J. Maultzsch, S. Reich, and C. Thomsen, *PHYSICAL REVIEW B* **74**, 115415 (2006).
- ²²B. S. Flavel, M. M. Kappes, R. Krupke, and F. Hennrich, *ACS Nano* **7**, 3557 (2013).
- ²³B. S. Flavel, K. E. Moore, M. Pfohl, M. M. Kappes, and F. Hennrich, *ACS Nano* **8**, 1817 (2014).
- ²⁴S. Lebedkin, F. Hennrich, T. Skipa, and M. M. Kappes, *Journal of Physical Chemistry B* **107**, 1949 (2003).
- ²⁵Y. Piao, J. R. Simpson, J. K. Streit, G. Ao, M. Zheng, J. A. Fagan, and A. R. Hight Walker, *ACS Nano* **10**, 5252 (2016).
- ²⁶S. M. Bachilo, M. S. Strano, C. Kittrell, R. H. Hauge, R. E. Smalley, and R. B. Weisman, *Science* **298**, 2361 (2002).
- ²⁷J. Jiang, R. Saito, G. G. Samsonidze, A. Jorio, S. G. Chou, G. Dresselhaus, and M. S. Dresselhaus, *PHYSICAL REVIEW B* **75**, 035407 (2007).
- ²⁸A. Jorio, A. G. Souza Filho, G. Dresselhaus, M. S. Dresselhaus, A. K. Swan, M. S. Ünlü, B. B. Goldberg, M. A. Pimenta, J. H. Hafner, C. M. Lieber, and R. Saito, *PHYSICAL REVIEW B* **65**, 155412 (2002).
- ²⁹P. Y. Yu and Y. R. Shen, *PHYSICAL REVIEW B* **12**, 1377 (1975).
- ³⁰A. V. Barzykin and M. Tachiya, *Physical Review B* **72**, 075425 (2005).